Available online at www.sciencedirect.com
ScienceDirect
Trans. Nonferrous Met. Soc. China 35(2025) 2699−2710
Transactions of Nonferrous Metals Society of China
www.tnmsc.cn

First-principles study on single metal anchored $CrSe_2$ for efficient electrocatalyst

Ya-dan SUN[1], Kun XIE[1], Pei SHI[1], Zhi-yan FENG[1], Long LIN[1,2]

1. Cultivating Base for Key Laboratory of Environment-Friendly Inorganic Materials in Henan Province, School of Materials Science and Engineering, Henan Polytechnic University, Jiaozuo 454000, China;
2. School of Mathematics and Informatics, Henan Polytechnic University, Jiaozuo 454000, China

Received 6 December 2023; accepted 27 May 2024

Abstract: To solve the problem of slow kinetics in oxygen reduction reaction (ORR) and oxygen evolution reaction (OER) and promote the development of bifunctional electrocatalysts, several two-dimensional $CrSe_2$-based single-atom catalysts (SACs) were constructed using 3d transition metal (TM) atoms. Density functional theory (DFT) was employed to explore the electrocatalytic mechanisms of ORR/OER. The results showed that most of the TM atoms prefer to be anchored at site H, and the negative binding energy proved the excellent structural stability of these SACs. The hybridization between the orbitals of O 2p and TM 3d contributes to the charge transfer. Furthermore, the 3d TM atoms can act as active sites to activate the adsorbates, thereby improving the catalytic efficiency of the substrate. Significantly, Ni/$CrSe_2$ exhibits the most outstanding ORR/OER catalytic performance, indicating its potential as a bifunctional electrocatalyst for ORR/OER.

Key words: density functional theory; $CrSe_2$; single atom catalyst; oxygen reduction reaction; oxygen evolution reaction

1 Introduction

Numerous environmental crises have occurred as the result of rising fossil fuel consumption, and the requirement for reliable and sustainable energy is particularly significant for the deteriorating environment [1,2]. Technologies including fuel cells, water splitting, and metal-air batteries have attracted more attention, but their efficiency is insufficient to satisfy the demands of large-scale applications [3,4]. Oxygen reduction reaction (ORR) and oxygen evolution reaction (OER) are the basis of these technologies, but the slow kinetic rates limit their advancement [5,6]. It is widely accepted that materials composed of precious metals can enhance ORR and OER activities, such as Pt-based materials and Ru/Ir oxides [7,8]. However, issues such as high price, scarcity, and poor stability have severely limited their utilization [9,10]. Therefore, the development of effective and sustainable ORR/OER electrocatalysts on non-noble substrates is of great importance in alleviating environmental problems [11,12].

Single-atom catalysts (SACs) are constructed by coordinating a single atom with the substrate atoms. Due to the unique structural properties and the exposure of active sites, SACs have become the frontier in catalysis with great significance for reducing the cost of catalysts and promoting the sustainable utilization of resources [13,14]. Through the investigations, the SACs constructed by 3d inexpensive transition metal (TM) atoms have outperformed stability and excellent electrocatalytic

Corresponding author: Long LIN, Tel: +86-18539153277, E-mail: linlong@hpu.edu.cn
https://doi.org/10.1016/S1003-6326(25)66841-5

performance, which is currently needed for the development of electrocatalysts with low cost, excellent stability, and high catalytic performance. XU et al [15] first successfully developed a stripping voltammetry method for quantitative analysis of 3d Cu SAC and showed that the catalyst has outstanding stability and ORR activity. CAO et al [16] developed a facile molten-salt-assisted emitting and trapping approach to construct 3d Fe single-atom catalysts and found that the resultant Fe-Z8NC&NaCl catalyst exhibits a remarkable activity and stability towards ORR. ZHANG et al [17] reported that the 3d TM-modified Mo_2B_2 SACs show excellent metallic conductivity. Among the candidates, Ni@Mo_2B_2 can be the candidate catalyst in hydrogen evolution reaction (HER) and OER, and Cu@Mo_2B_2 can effectively catalyze OER/ORR.

Two-dimensional material catalysts are widely used in the field of catalysis due to the characteristics of high utilization, excellent efficiency, and good selectivity [18−20]. Graphene [21], layered metal hydroxide (LDH) [22,23], hexagonal boron nitride (h-BN) [24], black phosphorous (BP) [25], and transition metal dichalcogenides (TMDs) [26] are examples. TMDs are a family of 2D layered materials that exhibit a "sandwich" structure with TM atoms layer located between the two chalcogen atoms layers [27,28], which are projected to be exploited as viable catalysts because of their inexpensive cost, simple synthesis, and comparable conductivity to noble metal-based catalysts [29,30]. WANG et al [31] constructed a heterostructure of spherical hollow WS_2 and petal-like MoS_2 and showed that the construction of heterostructures triggered the synergistic effect between WS_2 and MoS_2 and improved the HER performances. ZHOU et al [32] reported a strategy combining phase engineering and heteroatom doping, which can improve the electronic conductivity and active sites of $NiSe_2$, and promote its excellent activity in OER catalysis.

The outstanding advantages of two-dimensional TMD materials and the unique electronic structure of 3d SACs promoted the development of TMD-based SACs. However, there are no large-scale studies on the ORR/OER activities of TMD $CrSe_2$. The excellent conductivity of $CrSe_2$ [33] can facilitate the charge transfer in the reactions, which greatly stimulates our enthusiasm for the design of $CrSe_2$-based ORR/OER catalysts. Therefore, in this work, $CrSe_2$ was selected as the substrate to construct SACs by anchoring 3d TM atoms to explore the feasibility of the processes of ORR/OER. The first-principles calculation method based on density-functional theory (DFT) was employed to systematically investigate the structures, electronic properties, and electrocatalytic activities for ORR and OER of TM atoms anchored $CrSe_2$ (noted as TM/$CrSe_2$). Accordingly, the research is not only beneficial to develop alternatives for noble-metal materials catalysts, but also offers an in-depth understanding of the catalytic applications of TMD-based materials.

2 Computational methods

Spin-polarized density functional theory (DFT) was adopted to do all computations, which were run via the Vienna ab initio simulation package (VASP) [34]. The projector-augmented wave (PAW) pseudopotentials [35] were applied to characterizing the interactions between ions and electrons, and Perdew-Burke-Ernzerhof (PBE) functionals with generalized gradient approximation (GGA) were performed to describe the effects of electronic exchange-correlation [36]. By using the empirical correction, Grimme's DFT-D3 approach was adopted to correct the van der Waals interaction [37]. 400 eV was used as the cut-off energy for the plane-wave basis. The convergence limit for energy was set as 10^{-5} eV/atom, while the limit for force was set as 0.03 eV/Å. For the Brillouin zone integration, the Monkhorst-Pack (MP) approach for *k*-points was applied [38], with a 3×3×1 centered grid for geometric optimization and 7×7×1 for electronic properties. To eliminate the interactions between adjacent layers, a vacuum space of 20 Å in *z*-direction was introduced. The charge redistributions between the adsorbed O_2 and the SACs were described using Bader charge analysis [39]. To assess the strength of O—O bond interactions of the adsorbed O_2, the LOBSTER package-based crystal orbital Hamilton population (COHP) approach was adopted [40]. The thermostability of the high-performance SAC is verified by ab initio molecular dynamics (AIMD) simulations [41].

The stability of TM/$CrSe_2$ can be determined

by binding energy (E_b), which can be described by

$$E_b=E_{TM/CrSe_2}-E_{CrSe_2}-E_{TM} \quad (1)$$

where $E_{TM/CrSe_2}$ and E_{CrSe_2} denote the energy of TM anchored $CrSe_2$ and the intrinsic $CrSe_2$, respectively, and E_{TM} expresses the energy of a single TM atom in vacuum.

The cohesive energy (E_c) for the TM atoms in the bulk state can be defined as

$$E_c=E_{cell}/N-E_{TM} \quad (2)$$

where E_{cell} is the energy of the TM atom in bulk state, E_{TM} denotes the energy of single TM atom in vacuum, respectively, and N represents the number of TM atoms in the bulk phase.

The adsorption energy (E_{ads}) of O_2 adsorbed on TM/$CrSe_2$ SACs can be calculated by

$$E_{ads}=E_{TM/CrSe_2+O_2}-E_{TM/CrSe_2}-E_{O_2} \quad (3)$$

where $E_{TM/CrSe_2+O_2}$ and $E_{TM/CrSe_2}$ denote the energy of TM/$CrSe_2$ with and without the adsorption of O_2, and the energy of the free O_2 molecule is expressed by E_{O_2}.

The total reaction of ORR is $O_2+2H_2\rightarrow 2H_2O$, and OER goes reverse. The four-electron associative pathways of ORR were studied in detail. In theoretical calculations, the ORR through the four-electron reaction pathways is widely accepted [42], which follows the steps below:

$$*\xrightarrow{O_2+H^++e}OOH*\xrightarrow{+H^++e}O*+H_2O\xrightarrow{+H^++e}OH*\xrightarrow{+H^++e}*+H_2O \quad (4)$$

where * represents the active site, and OOH*, O* and OH* denote the oxygen-containing intermediates. The steps of OER can be carried out through the reverse processes.

The adsorption strength is explored to determine the catalytic activity of the catalyst by computing the adsorption energies (ΔE) as

$$\Delta E_{OOH*}=E_{OOH*}-E_*-(2E_{H_2O}-3/2E_{H_2}) \quad (5)$$

$$\Delta E_{O*}=E_{O*}-E_*-(E_{H_2O}-E_{H_2}) \quad (6)$$

$$\Delta E_{OH*}=E_{OH*}-E_*-(E_{H_2O}-1/2E_{H_2}) \quad (7)$$

To evaluate the ORR/OER catalytic activity of the TM/$CrSe_2$ SACs, the Gibbs free energy changes (ΔG) were calculated using the computational hydrogen electrode (CHE) method established by MAN et al [43]. The transformation of Gibbs free energy in the reaction from the reactant to the product is described by the formula as

$$\Delta G=\Delta E+\Delta E_{ZPE}-T\Delta S+\Delta G_U+\Delta G_{pH} \quad (8)$$

where ΔE and ΔE_{ZPE} stand for the calculated total energy changes and zero-point energy, respectively, and ΔS denotes the entropy between the reactants and the products. The temperature (T) is set as 298.15 K. $\Delta G_U=-neU$, where n stands for the number of transferred proton−electron pairs, e refers to the charge transferred, and U is the applied potential. $\Delta G_{pH}=k_BT\ln10\times pH$ is for determining the energy correction of proton concentration, in which k_B is Boltzmann constant, and pH=0 is considered according to the CHE model.

The reaction Gibbs free energy in each step (ΔG_i) for the formation of the intermediates correlates the potential determining steps, and can be calculated by $\Delta G_1=\Delta G_{OOH*}-4.92$ eV, $\Delta G_2=\Delta G_{O*}-\Delta G_{OOH*}$, $\Delta G_3=\Delta G_{OH*}-\Delta G_{O*}$, and $\Delta G_4=-\Delta G_{OH*}$, where G_*, G_{OOH*}, G_{O*} and G_{OH*} are the Gibbs free energies of the oxygen-containing intermediates. And in OER, $\Delta G_a=-\Delta G_4$, $\Delta G_b=-\Delta G_3$, $\Delta G_c=-\Delta G_2$, and $\Delta G_d=-\Delta G_1$.

The catalytic performance of the candidates can be expressed by overpotential, denoted as η, which follows the definitions below [44]:

$$\eta^{ORR}=\max\{\Delta G_1,\ \Delta G_2,\ \Delta G_3,\ \Delta G_4\}/e+1.23 \quad (9)$$

$$\eta^{OER}=\max\{\Delta G_a,\ \Delta G_b,\ \Delta G_c,\ \Delta G_d\}/e-1.23 \quad (10)$$

3 Results and discussion

3.1 Structure and stability of TM/$CrSe_2$

Figure 1(a) shows the optimized structure of the intrinsic 4×4×1 $CrSe_2$ supercell (48 atoms in total), with the Cr-layer located in the middle and the two Se-layers distributed on the two sides. Specifically, each Cr atom is coordinated with six Se atoms, Se atoms on both sides are in an "X−M" mode with Cr atoms. The lattice constant of the optimized $CrSe_2$ is 3.52 Å, which is consistent with the investigation by JIANG et al [45].

To acquire further insight into the electronic characteristics of the intrinsic $CrSe_2$, the density of states (DOS) and electronic band structures were calculated in a highly symmetric direction vacuum (Γ−M−K−Γ), as plotted in Fig. 1(b). It shows metallic characteristics, and there are some bands across the Fermi level. The total density of states

(TDOS) is mainly derived from the 3d electrons of Cr (orange line) and 4p electrons of Se (blue line). Distinctively, a significant hybridization interaction can be found between the orbitals of Cr 3d and Se 4p, expressing a strong interaction.

Since the unsatisfactory adsorption performance of O_2 on the intrinsic $CrSe_2$ (see Table S1 in Supplementary Materials, SM), TM modification is considered, and the selected 3d TM atoms are shown in Fig. 1(c). Structural relaxations were performed on the sites marked in Fig. 1(a), where Cr, Se and H denote the top site of the Cr atom, the top site of the Se atom, and the hollow site, respectively. The binding energy (E_b) of 3d TM on different sites of $CrSe_2$ was calculated by Eq. (1), as summarized in Table S2 of SM. All the E_b values are negative, indicating that these TM atoms can stably exist on the substrate and are expected to be further studied. By comparing the E_b on different sites, it can be concluded that Sc and Cu obtained the most negative binding energies at the Cr site, while Ti, V, Mn, Fe, Co and Ni are more favorable at the H site. The optimal structures with the lowest E_b are shown in Fig. 2.

Given that the TM atoms may form clusters on the substrate, and a high binding energy between the TM atom and the substrate could prevent it from aggregating into clusters. The cohesive energy (E_c) of the TM atom in the metallic bulk state was calculated by Eq. (2) to make a comparison with E_b,

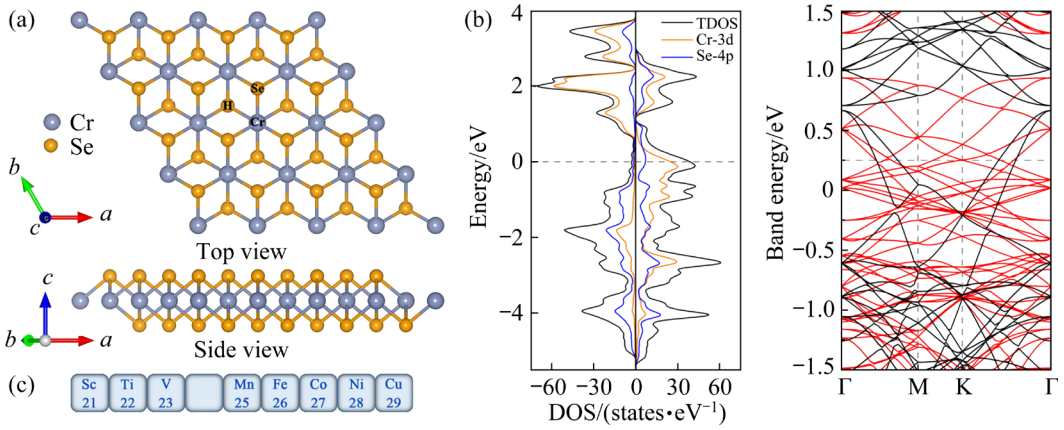

Fig. 1 (a) Structure of intrinsic $CrSe_2$ and considered anchoring sites; (b) DOS and electronic band structures of intrinsic $CrSe_2$; (c) Considered 3d TM atoms

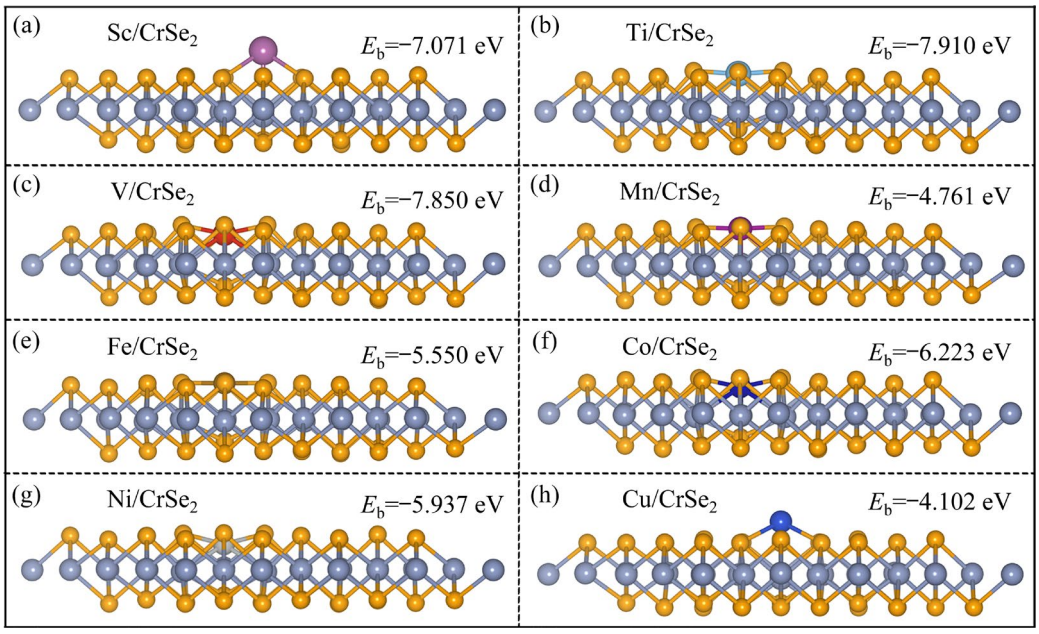

Fig. 2 Optimal structures of different $TM/CrSe_2$ (Sc and Cu: Cr site; Ti, V, Mn, Fe, Co and Ni: H site)

as listed in Table S2 of SM. The more negative the E_b is, the tighter the TM atom is anchored. And it is generally accepted as a stable configuration if E_b is more negative than E_c. A negative value of E_b−E_c indicates structural stability, implying that it is hard for the TM atom to form a cluster. As shown in Fig. 3(a), the lower area illustrates that E_b is more negative than E_c, while the value of E_b−E_c is positive in the upper area. It can be concluded that E_b−E_c is positive on Fe/$CrSe_2$ and Cu/$CrSe_2$ systems, while it is negative for Sc, Ti, V, Mn, Co, and Ni anchored systems, indicating that the formation of the cluster is difficult, thus proving the stability of these TM/$CrSe_2$ SACs.

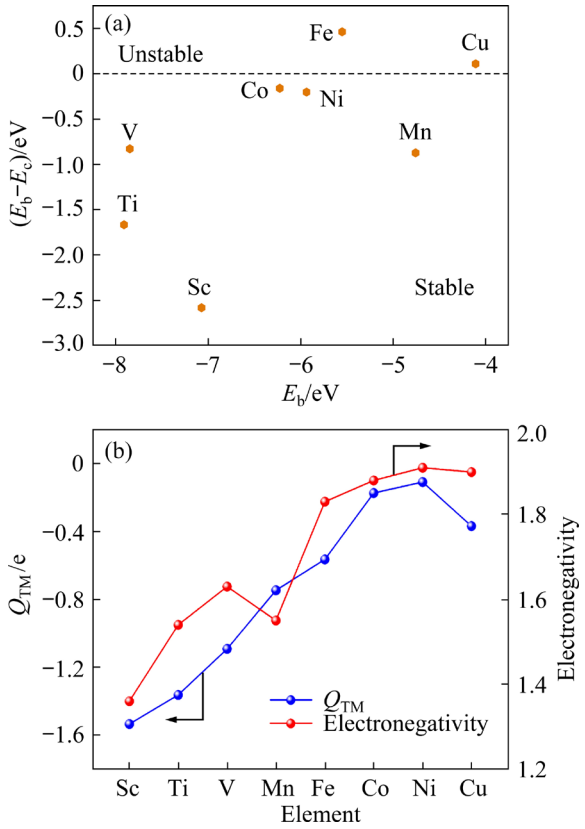

Fig. 3 (a) Relationship between E_b of TM atoms at most energetically favorable site and E_b−E_c; (b) Electronegativity and charge depletion (Q_{TM}) of TM

As shown in Table S2 of SM, there are different numbers of charges transferred from the 3d TM atom to the substrate, it is proved that the interaction exists between the introduced 3d TM atom and its coordinated atom. Therefore, the TM atom can be regarded as an electron donor, and can help tune the adsorption strength of the intermediates in the ORR/OER reactions. Among all the TM atoms, the Sc atom depletes the most charges (1.53 e), whereas the Ni atom donates the least (0.11 e). In addition, the amount of charge transferred gradually reduces as the atomic number increases, which is highly consistent with the general trend of electronegativity of the 3d TM atoms (Fig. 3(b)).

3.2 O_2 adsorption of TM/$CrSe_2$

To further explore the optimal configurations, the adsorption behaviors of O_2 both in side-on and end-on configurations were studied on Sc, Ti, V, Mn, Co, and Ni/$CrSe_2$ SACs with TM atom as the active site. The calculated E_{ads} (by Eq. (3)), O—O bond length and charges transferred to O_2 are shown in Table 1, where the positive ΔQ means charge accumulation.

Table 1 E_{ads} of O_2 on TM/$CrSe_2$ SACs, optimized d_{O-O}, and charges transferred to O_2 (ΔQ)

Catalyst	Configuration	E_{ads}/eV	d_{O-O}/Å	ΔQ/e
Sc/$CrSe_2$	Side-on	−1.371	1.445	0.961
	End-on	−0.815	1.311	0.654
Ti/$CrSe_2$	Side-on	−2.872	1.461	0.893
	End-on	−1.622	1.300	0.606
V/$CrSe_2$	Side-on	−2.503	1.441	0.784
	End-on	−1.699	1.284	0.618
Mn/$CrSe_2$	Side-on	−0.186	1.263	0.240
	End-on	−0.770	1.287	0.410
Co/$CrSe_2$	Side-on	−0.083	1.236	0.034
	End-on	−0.073	1.235	0.025
Ni/$CrSe_2$	Side-on	−0.946	1.330	0.429
	End-on	−0.086	1.286	0.318

It is important to point out that except for Mn/$CrSe_2$, the adsorption energy of O_2 is preferable when adsorbed in a side-on configuration. Besides, although Ni prefers to anchor at the H site, the adsorption of O_2 at the Cr site (−0.946 eV) is more favorable than that at the H site (0.054 eV), thus the properties for ORR/OER on the Cr site of Ni/$CrSe_2$ will be studied below. The E_{ads} on Co/$CrSe_2$ is too small to activate the adsorbed O_2, so the ORR process on Co/$CrSe_2$ will not be considered. The more negative of adsorption energy, the greater the elongation of d_{O-O}, and the larger amount of the charges transferred to the adsorbed O_2. All the optimal adsorption configurations of O_2 on candidates are depicted in Fig. S1 of SM.

As illustrated in Fig. 4, the bond lengths of O—O in O_2 molecules are elongated to various degrees on the surface of TM/$CrSe_2$ SACs, and are stretched to 1.445, 1.461, 1.441, 1.287, and 1.330 Å when adsorbed on Sc, Ti, V, Mn, and Ni-anchored systems (the initial O—O bond length is 1.234 Å), demonstrating that O_2 is activated to varying degrees. Additionally, the Bader charges calculations revealed that some charges transferred from the TM/$CrSe_2$ substrates to the adsorbed O_2 molecules (mainly provided by TM atoms), proving the chemical adsorption of O_2 molecules on the TM active center.

The partial density of states (PDOS) at the most energetically favorable structures was performed to explore the activation mechanism, and COHP analysis was utilized to investigate the bonding states of O—O bond in O_2. For comparison, the PDOS and COHP of O_2 in the free state are shown in Fig. 5(a). For more intuitive analysis, the −COHP plots are often constructed. The values of −COHP were considered, the region of −COHP>0 denotes bonding states, while −COHP<0 denotes antibonding states. From Figs. 5(b)−(f), the significant hybridization between O 2p and TM 3d reveals the strong interaction between O_2 and the TM atom. Compared with the free O_2, after the adsorption on TM/$CrSe_2$, the electron occupation of O 2p orbitals was generally moved to a more negative energy level because of the hybridization. It is noteworthy that more antibonding states (−COHP<0) appeared below the Fermi level after the adsorption, especially in the Ti and V decorated SACs, indicating the weakened strength of the O—O bond, which is also consistent with the larger value of the $|E_{ads}|$ and the more obvious stretching of O—O bond. And from the reduced integrated crystal orbital Hamilton population (ICOHP) (compared with the free O_2), it is again proved that the strength of O—O bond is weakened. Therefore, the candidates have the advantage of capturing and activating the adsorbed O_2 molecules.

3.3 ORR/OER catalytic activities

The unique geometric structures, excellent stability, and inherent excellent conductivity of these TM/$CrSe_2$ SACs greatly inspired us to assess the catalytic behavior towards ORR/OER processes. The catalytic performance of the candidates for ORR was first assessed. This work focuses on the associative mechanism, and the steps are as follows. Firstly, an O_2 molecule reacts with a proton to form OOH* with an electron transferred ($*+O_2+H^++e\rightarrow$ OOH*). Secondly, the intermediate OOH* is further hydrogenated and dissociated into O*, as a water molecule released ($OOH^*+H^++e\rightarrow O^*+H_2O$). Thirdly, O* is continuously adsorbing with a pair of (H^++e) and the OH* generated ($O^*+H^++e\rightarrow OH^*$). In the last step, the final product H_2O formed ($OH^*+H^++e\rightarrow H_2O$). The total reaction for ORR is: $O_2\rightarrow OOH^*\rightarrow O^*\rightarrow OH^*\rightarrow H_2O$, and OER follows reverse ($H_2O\rightarrow OH^*\rightarrow O^*\rightarrow OOH^*\rightarrow O_2$). Figure 6 depicts the reaction mechanism diagrams of the four-electron ORR and OER processes.

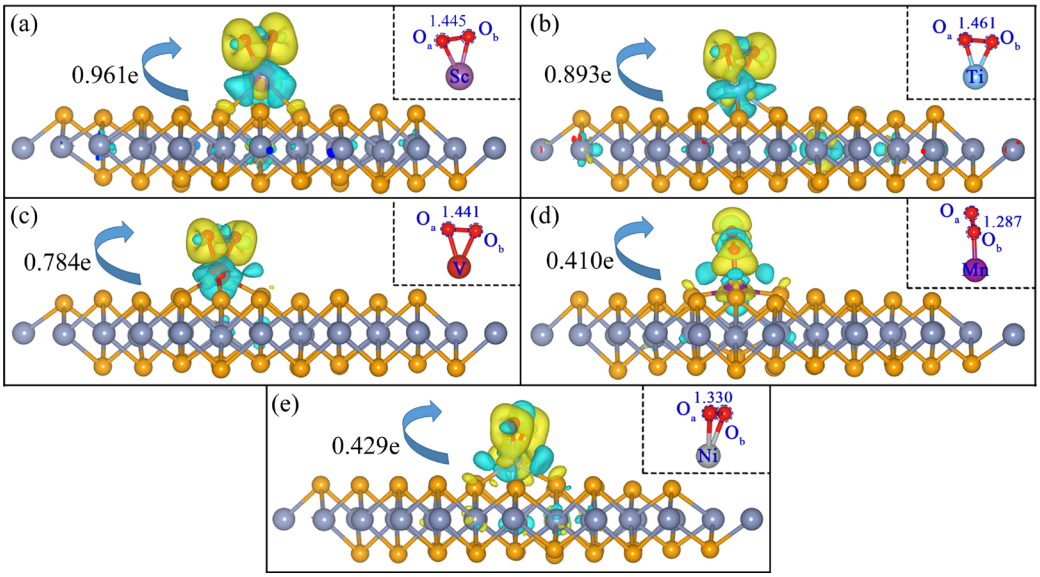

Fig. 4 Charge density difference on different SACs with O_2 adsorption (The green and yellow origins represent charge depletion and accumulation. The two atoms of O_2 are represented by O_a and O_b, respectively)

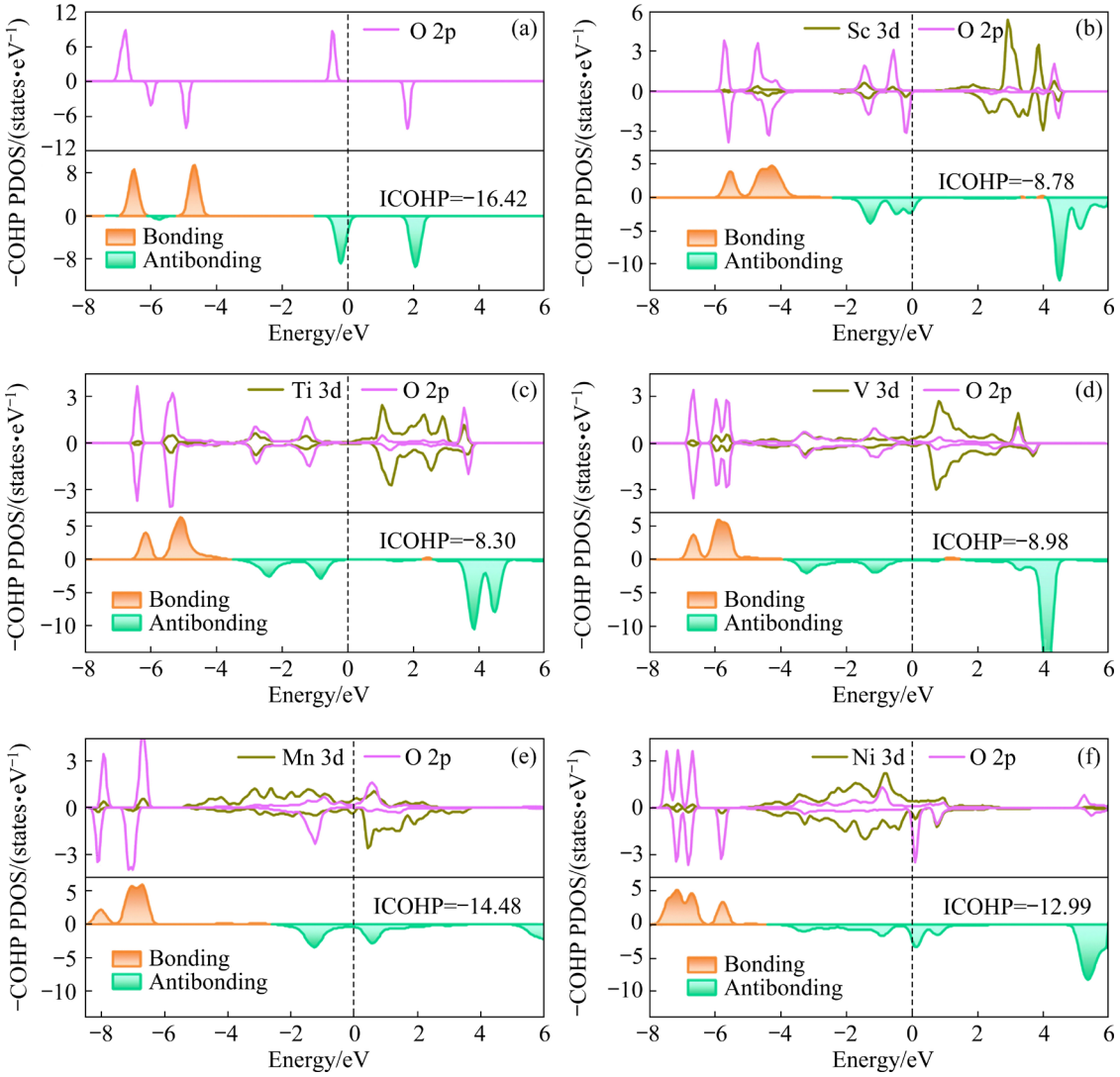

Fig. 5 (a) PDOS and COHP of free O_2; (b–f) PDOS of O_2 and TM atoms, as well as COHP analysis of O—O bond on TM/$CrSe_2$ surface

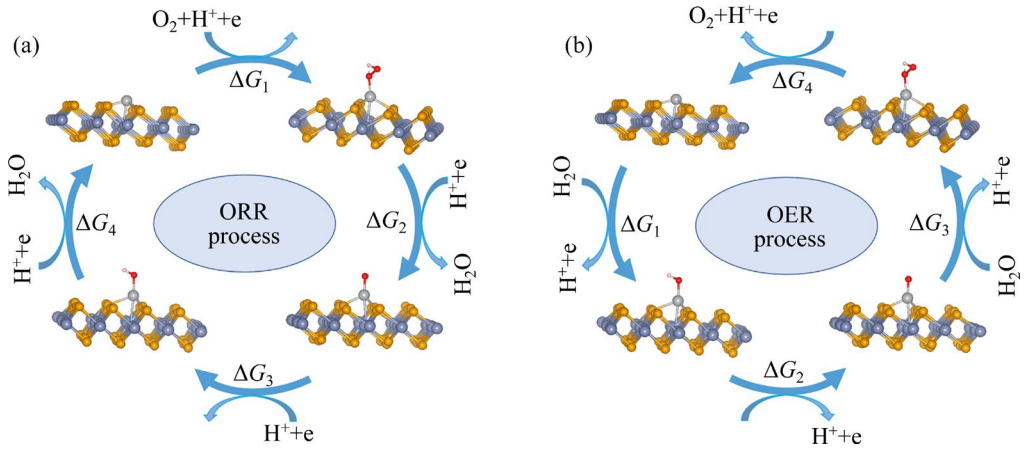

Fig. 6 Schematic diagrams of four-electron ORR (a) and OER (b) processes

The Sabatier principle states that moderate adsorption strength for all reactants and products are required for an optimal catalyst to ensure that the intermediates can transiently attach to the catalyst and can dissociate from the catalyst for another catalytic cycle. Therefore, the adsorption

behaviors of oxygen-containing intermediates are essential to investigate ORR and OER processes. Furthermore, the adsorption energies of intermediates are required to assess the catalytic activities of ORR/OER based on the CHE model. Therefore, before systematically evaluating the catalytic activity of TM/$CrSe_2$ for ORR and OER, the energetically favorable configuration of the oxygen-containing intermediates was investigated (Figs. S2−S6 in SM).

For ORR/OER, the change of Gibbs free energy (ΔG) in each fundamental reaction path determines the catalytic performance of a catalyst [46]. The potential-determining step (PDS) is recognized to be crucial since it determines the overpotential of a reaction. If ORR proceeds downhill, the minimum ΔG of the four elementary steps determines the ORR activities. As for OER, if it proceeds uphill, PDS corresponds to the largest ΔG. The relevant ΔG of each fundamental step on the candidate catalysts was computed along the mentioned reaction pathways to investigate the thermodynamics of ORR/OER processes, and the ΔG computed by Eq. (8) is presented in Table S4 of SM.

Based on the obtained ΔG, the Gibbs free energy profiles of ORR/OER on the five SACs candidates were plotted in Fig. 7. The PDSs for figuring out the activities of ORR and OER were marked in blue and green. As is evident from Fig. 7, the PDS of ORR on the active center of Sc, Ti, Mn, and Ni is the fourth step ($OH^*+H^++e\rightarrow H_2O$) under

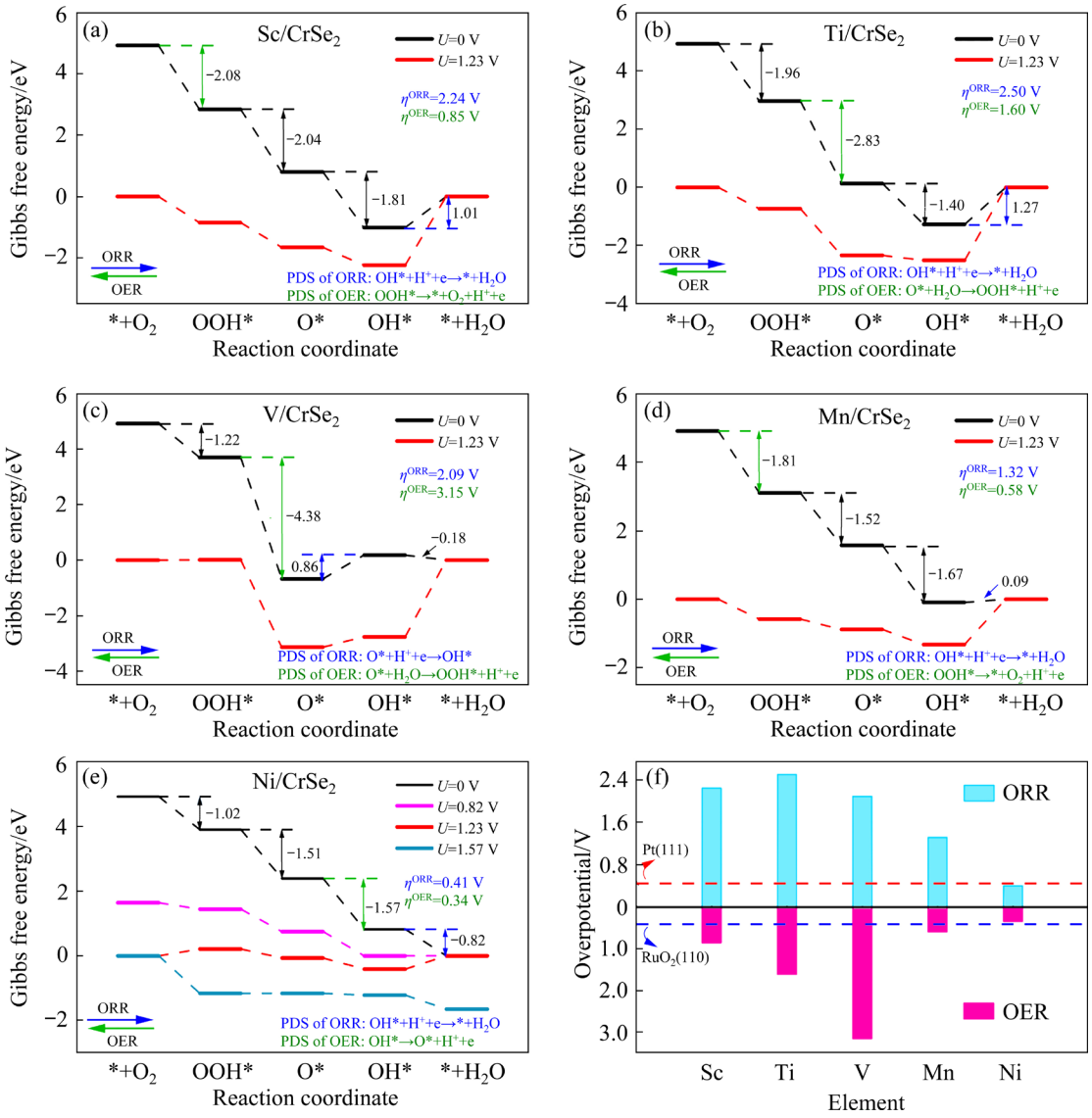

Fig. 7 Diagrams of Gibbs free energy for ORR and OER on Sc/$CrSe_2$, Ti/$CrSe_2$, V/$CrSe_2$, Mn/$CrSe_2$ and Ni/$CrSe_2$ (a−e), and overpotential of TM/$CrSe_2$ (f)

the applied potential of 0 V, whereas on V/$CrSe_2$, the PDS in ORR is the third step with the formation of OH*. The ORR steps on Ni/$CrSe_2$ are downhill, suggesting that the ORR reactions on Ni/$CrSe_2$ can happen spontaneously. When U is 1.23 V, the steps mentioned above become an upward trend, which is thermodynamically unfavorable. Sc, Ti, V, and Mn-anchored $CrSe_2$ exhibits low catalytic activity due to the larger barrier, which requires a higher external potential. Furthermore, the overpotentials can be obtained according to Eqs. (9) and (10), as shown in each diagram, among which Ni/$CrSe_2$ has the lowest ORR overpotential (0.41 V) due to its relatively smaller ΔG in the PDS (−0.82 eV). For the OER process, when U=0 V, the PDSs of Sc/$CrSe_2$ and Mn/$CrSe_2$ correspond to the last step of O_2 generation, with ΔG of 2.08 and 1.81 eV, respectively. The third step is the PDS on Ti and V anchored $CrSe_2$ with the Gibbs free energy barrier of 2.83 and 4.38 eV, while PDS for Ni/$CrSe_2$ is the second step with the formation of O*. When the applied U is 1.23 V, the determining step corresponds to the step with the largest rise in Gibbs free energy. Accordingly, the best catalyst for OER is Ni/$CrSe_2$ with the overpotential of 0.34 V. Therefore, the Gibbs free energy at $(1.23-\eta^{ORR})$ V and $(1.23+\eta^{OER})$ V for Ni/$CrSe_2$ are plotted in Fig. 7(e) for deeper analysis. The ORR steps are all downhill at 0 V and $(1.23-\eta^{ORR})$ V. The first and last steps become uphill at the potential of 1.23 V, with the maximum Gibbs free energy (ΔG_4) of 0.82 eV. On the other hand, all the fundamental steps in OER are uphill when U is 0 V, and it needs to ascend to proceed to the second and third steps under the applied U of 1.23 V. When U=1.23+η^{OER}, each step of the OER reaction is upward.

To compare the catalytic performance of candidates more intuitively, the η of ORR/OER is summarized in Fig. 7(f). The most advanced ORR catalyst Pt (111) and the best OER catalyst RuO_2 (110) are identified as the red and blue dashed lines. Our investigations suggest that the overpotentials for ORR/OER are 2.24/0.85, 2.50/1.60, and 2.09/3.15 V on Sc, Ti, and V anchored $CrSe_2$ SACs, respectively, indicating that these candidates cannot well catalyze the processes of ORR and OER. The reason for the extremely high overpotentials of ORR/OER on Sc, Ti, and V anchored $CrSe_2$ systems is the improper binding strength between the catalyst and the intermediates. In contrast, the catalytic performance of Mn/$CrSe_2$ has improved, especially for OER (η=0.58 V). Among all the SACs, it is noteworthy that the introduction of 3d Ni atom renders the system with outstanding bifunctional ORR/OER activities, with extremely low overpotentials of 0.41 and 0.34 V, close to and even lower than the precious metal-based catalysts such as Pt (0.45 V for ORR), RuO_2 (0.42 V for OER), as well as the metal-doped graphene materials, making it a promising bifunctional catalyst.

With 6000 steps (time step is 1 fs), the AIMD simulations of Ni/$CrSe_2$ were carried out at the temperatures of 300 and 500 K. As shown in Fig. 8, Ni/$CrSe_2$ retains its planar structure throughout the simulation procedure, no significant deformation is observed, and the total energy only fluctuates slightly. Therefore, Ni/$CrSe_2$ SAC screened in this work has outperformed thermodynamic stability and can be an efficient bifunctional ORR/OER catalyst.

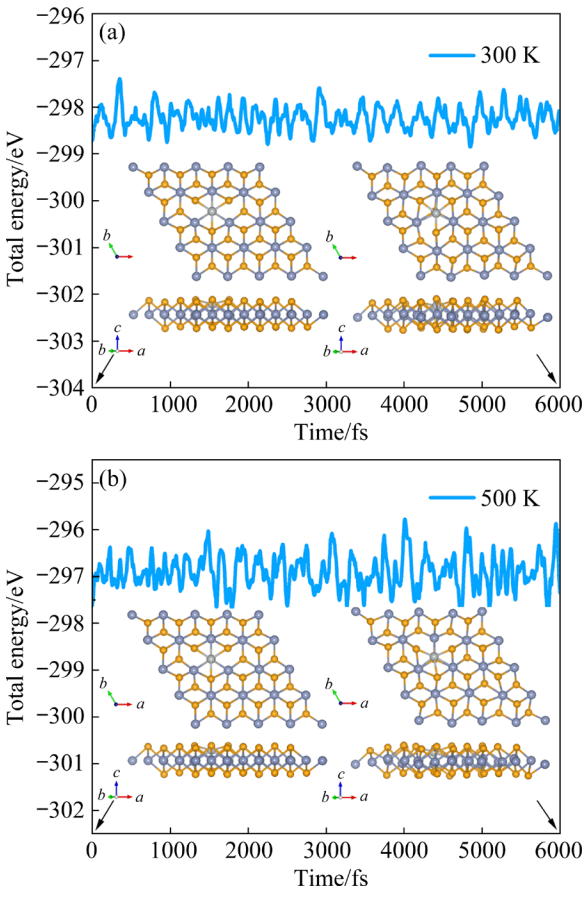

Fig. 8 AIMD simulations within 6000 fs for Ni/$CrSe_2$ at 300 K (a) and 500 K (b) (The atomic structures before and after the AIMD simulations are depicted)

4 Conclusions

(1) Most of the SACs (except for Fe/$CrSe_2$ and Cu/$CrSe_2$) exhibit structural stability, and the TM atom prefers to be attached to the H site.

(2) The candidate SACs have excellent electronic conductivity, which originates from the hybridization between orbitals of Cr 3d and Se 4p.

(3) The Bader charge analysis was employed to deeply understand the charge transfer, and it was proved that the TM atoms contribute to the charge accumulation on O_2.

(4) The introduction of the Ni atom renders Ni/$CrSe_2$ with moderate adsorption performance of intermediates, which makes it a promising bifunctional catalyst towards ORR/OER (η^{ORR}= 0.41 V, η^{OER}=0.34 V).

CRediT authorship contribution statement

Ya-dan SUN: Methodology, Investigation, Data curation, Writing – Original draft, Review & editing; **Kun XIE:** Methodology, Investigation; **Pei SHI:** Visualization, Methodology, Formal analysis, Writing – Review & editing; **Zhi-yan FENG:** Methodology, Data curation; **Long LIN:** Supervision, Resources, Conceptualization.

Declaration of competing interest

The authors declare that they have no known competing financial interests or personal relationships that could have appeared to influence the work reported in this paper.

Acknowledgments

This work was supported by the Key Project of NSFC-Henan Joint Fund (No. U2004209), and the National Natural Science Foundation of China (No. 21603109). Computational resources were provided by the Henan Polytechnic University high-performance grid computing platform, China.

Supplementary Materials

Supplementary Materials in this paper can be found at: http://tnmsc.csu.edu.cn/download/17-p2699-2023-1390-Supplementary_Materials.pdf.

References

[1] CHU S, CUI Y, LIU N. The path towards sustainable energy [J]. Nature Materials, 2017, 16: 16−22.

[2] ZHANG Si-xuan, HUANG Jin-zhao, DING Dian-jin, TANG Jun, DENG Xiao-long. Recent progress in NiMo-based amorphous alloys for electrocatalytic hydrogen evolution reaction [J]. Transactions of Nonferrous Metals Society of China, 2024, 34: 26−49.

[3] LI Hai-hua, YUAN Tie-chui, LI Rui-di, WANG Wen-jun, ZHEN Dan, YUAN Ji-wei. Electrochemical properties of powder-pressed Pb−Ag−PbO_2 anodes [J]. Transactions of Nonferrous Metals Society of China, 2019, 29: 2422−2429.

[4] CHUNG D Y, YOO J M, SUNG Y E. Highly durable and active Pt-based nanoscale design for fuel-cell oxygen-reduction electrocatalysts [J]. Advanced Materials, 2018, 30: 1704123.

[5] KHANI H, GRUNDISH N S, WIPF D O, GOODENOUGH J B. Graphitic-shell encapsulation of metal electrocatalysts for oxygen evolution, oxygen reduction, and hydrogen evolution in alkaline solution [J]. Advanced Energy Materials, 2020, 10: 1903215.

[6] LIAO Han-xiao, NI Gang-hai, TAN Peng-fei, LIU Kang, LIU Xuan-zhi, LIU He-le, CHEN Ke-jun, ZHENG Xu-sheng, LIU Min, PAN Jun. Oxyanion engineering suppressed iron segregation in nickel−iron catalysts toward stable water oxidation [J]. Advanced Materials, 2023, 35(21): 2300347.

[7] LI Yan-juan, WANG Min, LIU Sa, GAO Jing-xia, YANG Shun, LIU Zi-hao, LAI Xiao-yong, YAN Xiao. Preparation and properties of transition metal nitrides caged in N-doped hollow porous carbon sphere for oxygen reduction reaction [J]. Transactions of Nonferrous Metals Society of China, 2021, 31: 1427−1438.

[8] JIANG Min, ZHAI Huan-huan, CHEN Li-bao, MEI Lin, TAN Peng-fei, YANG Ke, PAN Jun. Unraveling the synergistic mechanism of bi-functional nickel–iron phosphides catalysts for overall water splitting [J]. Advanced Functional Materials, 2023, 33(33): 2302621.

[9] DUAN Ran, LI Ye-jun, WANG Shu, TONG Yong-gang, RUBAHN H G, ZHANG Gu-fei, QI Wei-hong. Effects of phosphate precursors on morphology and oxygen evolution reaction activity of NiFe (oxy)hydroxide on nickel foams [J]. Transactions of Nonferrous Metals Society of China, 2022, 32: 4050−4061.

[10] LIAO Han-xiao, LUO Tao, TAN Peng-fei, CHEN Ke-jun, LU Li-li, LIU Yong, LIU Min, PAN Jun. Unveiling role of sulfate ion in nickel−iron (oxy)hydroxide with enhanced oxygen-evolving performance [J]. Advanced Functional Materials, 2021, 31(38): 2102772.

[11] LIU Xuan-zhi, WANG Jian-chuan, LIAO Han-xiao, CHEN Jiao-yang, ZHANG Shao-hui, TAN Li-ming, ZHENG Xu-sheng, CHU De-wei, TAN Pen-fei, PAN Jun. Cationic oxidative leaching engineering modulated in situ self-reconstruction of nickel sulfide for superior water oxidation [J]. Nano Letters, 2023, 23: 5027−5034.

[12] PAN Yuan, ZHANG Chao, LIU Zhi, CHEN Chen, LI Ya-dong. Structural regulation with atomic-level precision: From single-atomic site to diatomic and atomic interface catalysis [J]. Matter, 2020, 2: 78−110.

[13] LIU Peng-xin, ZHAO Yun, QIN Rui-xuan, MO Shi-guang, CHEN Guang-xu, GU Lin, CHEVRIER D M, ZHANG Peng, GUO Qing, ZANG Dan-dan, WU Bing-hui, FU Gang, ZHENG Nan-feng. Photochemical route for synthesizing atomically dispersed palladium catalysts [J]. Science, 2016,

352(6287): 797−801.

[14] HAN Yong-dian, YANG Jia-hang, XU Lian-yong, JING Hong-yang, ZHAO Lei. Effect of transient current bonding on interfacial reaction in Ag-coated graphene Sn−Ag−Cu composite solder joints [J]. Transactions of Nonferrous Metals Society of China, 2021, 31: 2454−2467.

[15] XU Jing-song, LI Rui, XU Cong-qiao, ZENG Rong-guang, JIANG Zheng, MEI Bing-bao, LI Jun, MENG Da-qiao, CHEN Jun. Underpotential-deposition synthesis and in-line electrochemical analysis of single-atom copper electrocatalysts [J]. Applied Catalysis B, 2021, 289: 120028.

[16] CAO Yuan-jie, PENG Hao-yang, CHU Sheng-qi, TANG Yuan-ting, HUANG Chao-jun, WANG Zhi-li, LIU Feng, WU Jin-song, SHAN Bin, CHEN Rong. Molten-salt-assisted thermal emitting method to transform bulk Fe_2O_3 into Fe single atom catalysts for oxygen reduction reaction in Zn-air battery [J]. Chemical Engineering Journal, 2021, 420: 129713.

[17] ZHANG Tian, ZHANG Bi-kun, PENG Qiong, ZHOU Jian, SUN Zhi-mei. Mo_2B_2 MBene-supported single-atom catalysts as bifunctional HER/OER and OER/ORR electrocatalysts [J]. Journal of Materials Chemistry A, 2021, 9: 433−441.

[18] PANIGRAHI P, MISHRA S B, HUSSAIN T, NANDA B R K, AHUJA R. Density functional theory studies of Si_2BN nanosheets as anode materials for magnesium-ion batteries [J]. ACS Applied Nano Materials, 2020, 3: 9055−9063.

[19] GUO Xiang-yu, ZHANG Sheng-li, KOU Liang-zhi, YAM C Y, FRAUENHEIM T, CHEN Zhong-fang, HUANG Shi-ping. Data-driven pursuit of electrochemically stable 2D materials with basal plane activity toward oxygen electrocatalysis [J]. Energy & Environmental Science, 2023, 16: 5003−5018.

[20] TONGAY S, ZHOU Jian, ATACA C, LO K, MATTHEWS T S, LI Jing-bo, GROSSMAN J C, WU Jun-qiao. Thermally driven crossover from indirect toward direct bandgap in 2D semiconductors: $MoSe_2$ versus MoS_2 [J]. Nano Letters, 2012, 12: 5576−5580.

[21] QU Liang-ti, LIU Yong, BAEK J B, DAI Li-ming. Nitrogen-doped graphene as efficient metal-free electrocatalyst for oxygen reduction in fuel cells [J]. ACS Nano, 2010, 4: 1321−1326.

[22] LIAO Han-xiao, NI Gang-hai, TAN Peng-fei, LIU Yong, CHEN Ke-jun, WANG Gong-ming, LIU Min, PAN Jun. Borate narrowed band gap of nickel−iron layer double hydroxide to mediate rapid reconstruction kinetics for water oxidation [J]. Applied Catalysis B, 2022, 317: 121713.

[23] LI Lun, DOU Li-guang, ZHANG Hui. Layered double hydroxide supported gold nanoclusters by glutathione-capped Au nanoclusters precursor method for highly efficient aerobic oxidation of alcohols [J]. Nanoscale, 2014, 6: 3753−3763.

[24] LEE K H, SHIN H J, LEE J, LEE I Y, KIM G H, CHOI J Y, KIM S W. Large-scale synthesis of high-quality hexagonal boron nitride nanosheets for large-area graphene electronics [J]. Nano Letters, 2012, 12: 714−718.

[25] ZHANG Qing-zhe, HUANG Sheng-yun, DENG Jiu-jun, GANGADHARAN D T, YANG Fan, XU Zhen-he, GIORGI G, PALUMMO M, CHAKER M, MA Dong-ling. Ice-assisted synthesis of black phosphorus nanosheets as a metal-free photocatalyst: 2D/2D heterostructure for broadband H_2 evolution [J]. Advanced Functional Materials, 2019, 29: 1902486.

[26] VOIRY D, YANG J, CHHOWALLA M. Recent strategies for improving the catalytic activity of 2D TMD nanosheets toward the hydrogen evolution reaction [J]. Advanced Materials, 2016, 28: 6197−6206.

[27] CHEN Ren-jie, ZHAO Teng, WU Wei-ping, WU Feng, LI Li, QIAN Ji, XU Rui, WU Hui-ming, ALBISHRI H M, AL-BOGAMI A S, EL-HADY D A, LU Jun, AMINE K. Free-standing hierarchically sandwich-type tungsten disulfide nanotubes/graphene anode for lithium-ion batteries [J]. Nano Letters, 2014, 14: 5899−5904.

[28] SHU Hai-bo, LI Feng, HU Chen-li, LIANG Pei, CAO Dan, CHEN Xiao-shuang. The capacity fading mechanism and improvement of cycling stability in MoS_2-based anode materials for lithium-ion batteries [J]. Nanoscale, 2016, 8: 2918−2926.

[29] WANG Feng-mei, SHIFA T A, ZHAN Xue-ying, HUANG Yun, LIU Kai-li, CHENG Zhong-zhou, JIANG Chao, HE Jun. Recent advances in transition-metal dichalcogenide based nanomaterials for water splitting [J]. Nanoscale, 2015, 7: 19764−19788.

[30] HOU Yang, ZHUANG Xiao-dong, FENG Xin-liang. Recent advances in earth-abundant heterogeneous electrocatalysts for photoelectrochemical water splitting [J]. Small Methods, 2017, 1: 1700090.

[31] WANG De-zhi, YANG Liu-yi-yi, LIU Ruo-qi, GUO Ting, FEI Hao, WU Zhuang-zhi. Preparation and electrocatalytic hydrogen evolution performance of spherical hollow MoS_2/WS_2 heterostructures [J]. Transactions of Nonferrous Metals Society of China, 2023, 33: 1540−1549.

[32] ZHOU Jun, YUAN Li-wei, WANG Jing-wen, SONG Ling-ling, YOU Yu, ZHOU Ru, ZHANG Jun-jun, XU Jun. Combinational modulations of $NiSe_2$ nanodendrites by phase engineering and iron-doping towards an efficient oxygen evolution reaction [J]. Journal of Materials Chemistry A, 2020, 8: 8113−8120.

[33] WANG Jin-song, LIU Jia, ZHANG Bao, JI Xiao, XU Kui, CHEN Chi, MIAO Ling, JIANG Jian-jun. The mechanism of hydrogen adsorption on transition metal dichalcogenides as hydrogen evolution reaction catalyst [J]. Physical Chemistry Chemical Physics, 2017, 19: 10125−10132.

[34] KRESSE G, FURTHMÜLLER J. Efficient iterative schemes for ab initio total-energy calculations using a plane-wave basis set [J]. Physical Review B, 1996, 54: 11169−11186.

[35] KRESSE G, JOUBERT D. From ultrasoft pseudopotentials to the projector augmented-wave method [J]. Physical Review B, 1999, 59: 1758−1775.

[36] PERDEW J P, WANG Yue. Accurate and simple density functional for the electronic exchange energy: Generalized gradient approximation [J]. Physical Review B, 1986, 33: 8800−8802.

[37] GRIMME S. Semiempirical GGA-type density functional constructed with a long-range dispersion correction [J]. Journal of Computational Chemistry, 2006, 27: 1787−1799.

[38] CHADI D J. Special points for Brillouin-zone integrations [J]. Physical Review B, 1976, 16: 1746−1747.

[39] TANG Wen-jie, SANVILLE E, HENKELMAN G. A

grid-based Bader analysis algorithm without lattice bias [J]. Journal of Physics: Condensed Matter, 2009, 21: 084204.

[40] NELSON R, ERTURAL C, GEORGE J, DERINGER V L, HAUTIER G, DRONSKOWSKI R. LOBSTER: Local orbital projections, atomic charges, and chemical-bonding analysis from projector-augmented-wave-based density-functional theory [J]. Journal of Computational Chemistry, 2020, 41: 1931−1940.

[41] TUCKERMAN M, LAASONEN K, SPRIK M, PARRINELLO M. Ab initio molecular dynamics simulation of the solvation and transport of hydronium and hydroxyl ions in water [J]. The Journal of Chemical Physics, 1995, 103: 150−161.

[42] ZENG Hang-hang, LIU Xin-yi, CHEN Feng-bo, CHEN Zhi-guo, FAN Xiao-li, LAU W. Single atoms on a nitrogen-doped boron phosphide monolayer: A new promising bifunctional electrocatalyst for ORR and OER [J]. ACS Applied Materials & Interfaces, 2020, 12: 52549−52559.

[43] MAN I C, SU H Y, VALLEJO F C, HANSEN H A, MARTÍNEZ J I, INOGLU N G, KITCHIN J, JARAMILLO T F, NØRSKOV J K, ROSSMEISL J. Universality in oxygen evolution electrocatalysis on oxide surfaces [J]. ChemCatChem, 2011, 3: 1159−1165.

[44] ZHANG Wen-qing, WANG Juan, ZHAO Lan-ling, WANG Jun-ru, ZHAO Ming-wen. Transition-metal monochalcogenide nanowires: High-efficient bi-functional catalysts for the oxygen evolution/reduction reactions [J]. Nanoscale, 2020, 12: 12883−12890.

[45] JIANG Cun-yuan, YANG Zhi-yao, XIONG Wen, WANG Fei. Effect of strain engineering on magnetism-induced valley splitting in WSe_2 based on the $WSe_2/CrSe_2$ heterojunction [J]. Applied Physics Letters, 2021, 119: 162101.

[46] QIN Zeng-ming, ZHAO Jing-xiang. 1T-$MoSe_2$ monolayer supported single Pd atom as a highly-efficient bifunctional catalyst for ORR/OER [J]. Journal of Colloid and Interface Science, 2022, 605: 155−162.

单金属锚定 $CrSe_2$ 用于高效电催化剂的第一性原理研究

孙亚丹[1]，解 坤[1]，石 佩[1]，冯志研[1]，林 龙[1,2]

1. 河南理工大学 材料科学与工程学院 河南省环境友好无机材料重点实验室培育基地，焦作 454000；
2. 河南理工大学 数学与信息科学学院，焦作 454000

摘 要：为了解决氧还原反应(ORR)和析氧反应(OER)中动力学缓慢的问题，促进双功能电催化剂的发展，利用 3d TM 原子构筑了几种二维 $CrSe_2$ 基单原子催化剂(SACs)。采用密度泛函理论(DFT)研究氧还原反应/析氧反应的电催化机理。结果表明，大多数 TM 原子倾向于锚定在位点 H 上，负的结合能证明了 SACs 优异的结构稳定性。O 2p 与 TM 3d 轨道之间的杂化有助于电荷转移。此外，3d TM 原子可以作为活性位点来活化吸附物质，从而提高基底的催化效率。值得注意的是，Ni/$CrSe_2$ 表现出优异的氧还原反应/析氧反应催化性能，表明其作为氧还原反应/析氧反应的双功能电催化剂的潜力。

关键词：密度泛函理论；$CrSe_2$；单原子催化剂；氧还原反应；析氧反应

(Edited by Xiang-qun LI)